

Evolution of Physical and Photocatalytic Properties in the Layered Titanates $\text{A}_2\text{Ti}_4\text{O}_9$ ($\text{A} = \text{K}, \text{H}$) and in Nanosheets Derived by Chemical Exfoliation[†]

Mark R. Allen,[‡] Arthur Thibert,[‡] Erwin M. Sabio,[‡] Nigel D. Browning,^{§,||}
Delmar S. Larsen,[‡] and Frank E. Osterloh*,[‡]

[‡]Department of Chemistry and [§]Department of Materials Science and Engineering, University of California, One Shields Avenue, Davis, California 95616, and ^{||}Lawrence Livermore National Laboratory, 7000 East Avenue, Livermore, California 94550

Received August 31, 2009. Revised Manuscript Received October 7, 2009

$\text{K}_2\text{Ti}_4\text{O}_9$ has been known as a photocatalyst for the oxidation of methanol under UV irradiation. Here we study the evolution of morphology, optical, and photocatalytic properties of this titanate as it is converted into $\text{H}_2\text{Ti}_4\text{O}_9$ and subsequently exfoliated into individual tetrabutylammonium (TBA)-supported $[\text{Ti}_4\text{O}_9]^{2-}$ nanosheets. We find that proton exchange and exfoliation are accompanied by a red shift of the optical absorption edge and fluorescence maximum, suggesting a reduction of the bandgap in the series $\text{K}_2\text{Ti}_4\text{O}_9$ (3.54 eV), $\text{H}_2\text{Ti}_4\text{O}_9$ (3.25 eV), TBA₂ Ti_4O_9 (3.00 eV). Neither compound is active for photochemical water splitting, even after photochemical deposition of platinum nanoparticles. However, in aqueous methanol, all platinated compounds are moderately active for H_2 evolution upon bandgap irradiation, and in 0.01 M AgNO_3 , they all produce moderate quantities of O_2 . From the onset potentials for photoelectrochemical methanol oxidation, the values for the valence band edges at pH = 7 are deduced to lie between -0.23 and -0.53 V (NHE) for the nonplatinated compounds, and at +0.08 V and -0.30 V for the platinated compounds. This Pt-induced decrease of negative charge on the titanates is likely due to Fermi level equilibration of metal and semiconductor. Its effect can also be seen in a shift of the onset potentials for electrochemical water oxidation, as measured by cyclic voltammetry. Transient absorption data reveal that photogenerated electrons become trapped in mid band gap states, from which they decay exponentially with a time-constant of 43.67 ± 0.28 ms, much slower than observed for 68 ± 1 ns for TiO_2 nanocrystals (Degussa, P25).

Introduction

Direct photoelectrolysis of water is a promising pathway for the conversion of abundant photochemical energy into hydrogen, an environmentally sound fuel. The reaction is catalyzed by group IV and V metal oxides, often in combination with group 9 or 10 metal and metal oxide cocatalysts.¹ The major obstacle for commercial systems is that none of the known catalysts reaches energy conversion efficiencies above 1%. This is generally attributed to ineffective photochemical charge separation and significant overpotentials for water redox reactions on surfaces. To develop better catalysts, we recently began an investigation of the photocatalytic properties of metal

oxide and metal chalcogenide nanosheets.^{2–7} Metal oxide nanosheets can be obtained chemically by exfoliation of layered oxide precursors, including the Dion-Jacobsen phase $\text{KCa}_2\text{Nb}_3\text{O}_{10}$ and $\text{K}_4\text{Nb}_6\text{O}_{17}$.^{8–12} As single-crystalline fragments of the bulk phases, these nanosheets can be regarded as model catalysts that can provide insight into mechanistic aspects of water photoelectrolysis, including excited state lifetimes, reaction intermediates, electrochemical reactivity, and band edge potentials. Furthermore, because of their nanoscale dimensions,

[†]Accepted as part of the 2010 “Materials Chemistry of Energy Conversion Special Issue”.

*Corresponding author. Fax: (+1) 530 752 8995. Tel: (+1) 530 752 6242. E-mail: fosterloh@ucdavis.edu.

(1) Osterloh, F. E. *Chem. Mater.* **2008**, *20*(1), 35–54.

(2) Compton, O. C.; Osterloh, F. E. *J. Phys. Chem. C* **2009**, *113*(1), 479–485.

(3) Sarahan, M. C.; Carroll, E. C.; Allen, M.; Larsen, D. S.; Browning, N. D.; Osterloh, F. E. *J. Solid State Chem.* **2008**, *181*(7), 1681–1686.

(4) Frame, F. A.; Carroll, E. C.; Larsen, D. S.; Sarahan, M. S.; Browning, N. D.; Osterloh, F. E. *Chem. Commun.* **2008**, 2206–2208.

- (5) Compton, O. C.; Mullet, C. H.; Chiang, S.; Osterloh, F. E. *J. Phys. Chem. C* **2008**, *112*(15), 6202–6208.
(6) Carroll, E. C.; Compton, O. C.; Madsen, D.; Larsen, D. S.; Osterloh, F. E. *J. Phys. Chem. C* **2008**, *112*(7), 2394–2403.
(7) Compton, O. C.; Carroll, E. C.; Kim, J. Y.; Larsen, D. S.; Osterloh, F. E. *J. Phys. Chem. C* **2007**, *111*(40), 14589–14592.
(8) Jacobsen, A. J.; Johnson, J. W.; Lewandowski, J. T. *Inorg. Chem.* **1985**, *24*, 3727–3729.
(9) Treacy, M. M. J.; Rice, S. B.; Jacobson, A. J.; Lewandowski, J. T. *Chem. Mater.* **1990**, *2*(3), 279–286.
(10) Miyamoto, N.; Yamamoto, H.; Kaito, R.; Kuroda, K. *Chem. Commun.* **2002**, *20*, 2378–2379.
(11) Saupe, G. B.; Waraksa, C. C.; Kim, H.-N.; Han, Y. J.; Kaschak, D. M.; Skinner, D. M.; Mallouk, T. E. *Chem. Mater.* **2000**, *12*(6), 1556–1562.
(12) Matsumoto, Y.; Koinuma, M.; Iwanaga, Y.; Sato, T.; Ida, S. *J. Am. Chem. Soc.* **2009**, *131*(19), 6644–6645.

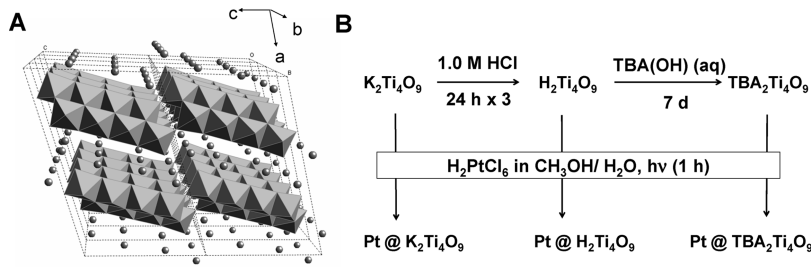


Figure 1. Crystal structure of $\text{K}_2\text{Ti}_4\text{O}_9$ and synthetic scheme for the preparation of titanates.

these nanocrystals are theoretically expected to have enhanced catalytic properties. Charge transport pathways are short, reducing problems arising from ohmic resistance and short excited state lifetimes. At the same time the surface area is high, maximizing reaction rates with water.

Here we extend our studies on the photocatalytic properties of nanometal oxides to nanosheets derived from the layered phase $\text{K}_2\text{Ti}_4\text{O}_9$. As a member of the series $\text{M}_2\text{O} \cdot n\text{TiO}_2$ ($\text{M} = \text{Na}, \text{K}, \text{Rb}, \text{Cs}, \text{Tl}$), with $n = 0.5, 1.0$, or 2.0 ,¹³ $\text{K}_2\text{Ti}_4\text{O}_9$ ($n = 4$, Figure 1) consists of layers of edge- and corner-shared TiO_6 octahedra, which are separated by layers of K ions.^{14,15} Because of corner sharing of the some of the TiO_6 octahedra, the sheets form step edges parallel to the b direction in the crystal.

Structurally, $\text{K}_2\text{Ti}_4\text{O}_9$ is also related to a variety of titanium oxides that are active catalysts for the photochemical water splitting reaction, including TiO_2 ,^{16–21} SrTiO_3 ,^{22–25} La_2TiO_5 and $\text{La}_2\text{Ti}_3\text{O}_9$,²⁶ $\text{La}_2\text{Ti}_2\text{O}_7$,^{27,28} $\text{Sr}_3\text{Ti}_2\text{O}_7$,²⁹

- (13) Tournoux, M.; Marchand, R.; Brohan, L. *Prog. Solid State Chem.* **1986**, *17*(1), 33–52.
- (14) Berry, K. L.; Aftandilian, V. D.; Gilbert, W. W.; Meibohm, E. P. H.; Young, H. S. *J. Inorg. Nucl. Chem.* **1960**, *14*(3–4), 231–239.
- (15) Dion, M.; Piffard, Y.; Tournoux, M. *J. Inorg. Nucl. Chem.* **1978**, *40*(5), 917–918.
- (16) Schrauzer, G. N.; Guth, T. D. *J. Am. Chem. Soc.* **1977**, *99*(22), 7189–7193.
- (17) Sato, S.; White, J. M. *Chem. Phys. Lett.* **1980**, *72*(1), 83–86.
- (18) Duonghong, D.; Borgarello, E.; Gratzel, M. *J. Am. Chem. Soc.* **1981**, *103*(16), 4685–4690.
- (19) Yamaguti, K.; Sato, S. *J. Chem. Soc., Faraday Trans. I* **1985**, *81*, 1237–1246.
- (20) Abe, R.; Sayama, K.; Domen, K.; Arakawa, H. *Chem. Phys. Lett.* **2001**, *344*(3–4), 339–344.
- (21) Abe, R.; Sayama, K.; Sugihara, H. *J. Phys. Chem. B* **2005**, *109*(33), 16052–16061.
- (22) Domen, K.; Naito, S.; Soma, M.; Onishi, T.; Tamari, K. *J. Chem. Soc., Chem. Commun.* **1980**, *12*, 543–544.
- (23) Domen, K.; Naito, S.; Onishi, T.; Tamari, K. *Chem. Phys. Lett.* **1982**, *92*(4), 433–434.
- (24) Lehn, J. M.; Sauvage, J. P.; Ziessel, R. *New J. Chem.* **1980**, *4*(11), 623–627.
- (25) Lehn, J. M.; Sauvage, J. P.; Ziessel, R.; Hilaire, L. *Israel J. Chem.* **1982**, *22*(2), 168–172.
- (26) Kim, J.; Hwang, D. W.; Kim, H. G.; Bae, S. W.; Lee, J. S.; Li, W.; Oh, S. H. *Top. Catal.* **2005**, *35*(3–4), 295–303.
- (27) Abe, R.; Higashi, M.; Sayama, K.; Abe, Y.; Sugihara, H. *J. Phys. Chem. B* **2006**, *110*(5), 2219–2226.
- (28) Kim, H. G.; Hwang, D. W.; Kim, J.; Kim, Y. G.; Lee, J. S. *Chem. Commun.* **1999**, *12*, 1077–1078.
- (29) Jeong, H.; Kim, T.; Kim, D.; Kim, K. *Int. J. Hydrogen Energ.* **2006**, *31*(9), 1142–1146.
- (30) Kim, H. G.; Becker, O. S.; Jang, J. S.; Ji, S. M.; Borse, P. H.; Lee, J. S. *J. Solid State Chem.* **2006**, *179*(4), 1214–1218.
- (31) Takata, T.; Furumi, Y.; Shinohara, K.; Tanaka, A.; Hara, M.; Kondo, J. N.; Domen, K. *Chem. Mater.* **1997**, *9*, (5), 1063–&.
- (32) Gopalakrishnan, J.; Bhat, V. *Inorg. Chem.* **1987**, *26*(26), 4299–4301.
- (33) Kudo, A.; Sakata, T. *J. Phys. Chem.* **1995**, *99*(43), 15963–15967.

PbTiO_3 ,³⁰ $\text{M}_2\text{La}_2\text{Ti}_3\text{O}_{10}$ ($\text{M} = \text{K}, \text{Rb}, \text{Cs}$),^{31–35} $\text{PbBi}_4\text{Ti}_4\text{O}_{15}$,³⁰ BaTi_4O_9 ,^{36,37} the tunnel titanates $\text{M}_2\text{Ti}_6\text{O}_{13}$ ($\text{M} = \text{Na}, \text{K}, \text{Rb}$),^{36,38} and $\text{La}_4\text{CaTi}_5\text{O}_{17}$,²⁸

$\text{K}_2\text{Ti}_4\text{O}_9$ itself has been investigated as a photocatalyst for photochemical phenol decomposition,³⁹ and nanosheets derived from $\text{K}_2\text{Ti}_4\text{O}_9$ were studied by Izawa et al.⁴⁰ for photoelectrochemical methanol oxidation. Of several $\text{H}_2\text{Ti}_4\text{O}_9$ – TiO_2 composites tested by Sato's group, $\text{H}_2\text{Ti}_4\text{O}_9$ itself was found to be inactive for the photochemical water splitting reaction,⁴¹ even though a $\text{H}_2\text{Ti}_4\text{O}_9$ – Fe_2O_3 composite did evolve H_2 from aqueous Na_2SO_3 solution under visible light irradiation.⁴² Finally, $\text{K}_2\text{Ti}_4\text{O}_9$ was employed by Mallouk and co-workers as water reduction catalyst in combination with a Ru-dye as sensitizer.⁴³

As we will show here, the optical, electronic, and photocatalytic properties $\text{K}_2\text{Ti}_4\text{O}_9$ remain largely intact as the compound is converted from a crystalline solid into individually dispersed nanosheets. This means that optical excitation, charge separation, and water activation likely occur on individual titanate layers, and do not involve interlayer charge transfer. We also find that photochemical platination causes a significant shift of the edge potentials to more positive values, which we interpret as a consequence of Fermi level equilibration between the metal and semiconductor.

Results and Discussion

Figure 1B gives an overview over the preparation of compounds relevant to this work. $\text{K}_2\text{Ti}_4\text{O}_9$ was synthesized according to the literature by heating TiO_2 with a 10% stoichiometric excess of K_2CO_3 to 960 °C for 10 h.

- (34) Takata, T.; Shinohara, K.; Tanaka, A.; Hara, M.; Kondo, J. N.; Domen, K. *Photochem. Photobiol. A* **1997**, *106*(1–3), 45–49.
- (35) Ikeda, S.; Hara, M.; Kondo, J. N.; Domen, K.; Takahashi, H.; Okubo, T.; Kakihana, M. *Chem. Mater.* **1998**, *10*(1), 72–77.
- (36) Inoue, Y. Water Photolysis by Titanates with Tunnel Structures. In *Photocatalysis Science and Technology*; Kaneko, M., Okura, I., Eds.; Springer: New York, 2002; pp 249–260.
- (37) Inoue, Y.; Niijima, T.; Asai, Y.; Sato, K. *J. Chem. Soc., Chem. Commun.* **1992**, *7*, 579–580.
- (38) Ogura, S.; Kohno, M.; Sato, K.; Inoue, Y. *Appl. Surf. Sci.* **1997**, *121*, 521–524.
- (39) Cheng, S. F.; Tsai, S. J.; Lee, Y. F. *Catal. Today* **1995**, *26*(1), 87–96.
- (40) Izawa, K.; Yamada, T.; Unal, U.; Ida, S.; Altuntasoglu, O.; Koinuma, M.; Matsumoto, Y. *J. Phys. Chem. B* **2006**, *110*(10), 4645–4650.
- (41) Uchida, S.; Yamamoto, Y.; Fujishiro, Y.; Watanabe, A.; Ito, O.; Sato, T. *J. Chem. Soc., Faraday Trans.* **1997**, *93*(17), 3229–3234.
- (42) Sato, T.; Yamamoto, Y.; Fujishiro, Y.; Uchida, S. *J. Chem. Soc., Faraday Trans.* **1996**, *92*(24), 5089–5092.
- (43) Kim, Y. I.; Atherton, S. J.; Brigham, E. S.; Mallouk, T. E. *J. Phys. Chem.* **1993**, *97*(45), 11802–11810.

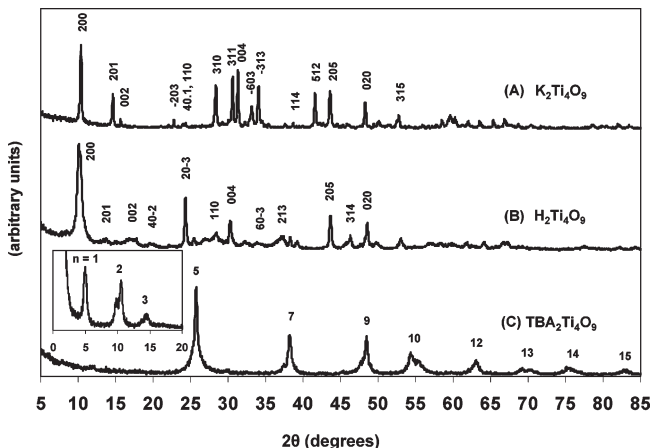


Figure 2. Powder XRD of (A) $\text{K}_2\text{Ti}_4\text{O}_9$, (B) $\text{H}_2\text{Ti}_4\text{O}_9 \cdot \text{H}_2\text{O}$, and (C) $\text{TBA}_2\text{Ti}_4\text{O}_9$. Peak assignments follow pdf card 32–0861 for $\text{K}_2\text{Ti}_4\text{O}_9$, and ref 41 for $\text{H}_2\text{Ti}_4\text{O}_9 \cdot \text{H}_2\text{O}$. Inset shows diffraction peaks for $\text{TBA}_2\text{Ti}_4\text{O}_9$ film obtained by drop coating/evaporation.

The resulting white powder was then converted into $\text{H}_2\text{Ti}_4\text{O}_9$ by reaction with 1.0 M aqueous HCl over the course of several days. Exfoliated tetrabutylammonium-(TBA)-stabilized nanosheets were obtained by stirring a suspension of $\text{H}_2\text{Ti}_4\text{O}_9$ with 13.3% TBA hydroxide in water for 7.5 days. A different procedure using ethylamine had been previously reported in the literature.⁴⁴

XRD data of all phases are shown in Figure 2. The diffraction peaks for $\text{K}_2\text{Ti}_4\text{O}_9$ are in accordance with the literature pattern.^{14,15} The pattern obtained for the proton exchanged phase agrees with the reported pattern for the monohydrate $\text{H}_2\text{Ti}_4\text{O}_9 \times \text{H}_2\text{O}$.^{41,42,45} The XRD pattern of the dried TBA exfoliated phase is shown in Figure 2C, with the inset showing the XRD of a film of the same material. In $\text{TBA}_2\text{Ti}_4\text{O}_9$, all reflections of $\text{H}_2\text{Ti}_4\text{O}_9$ are replaced by a new set of peaks, which can be assigned to intersheet reflections of a lamellar phase, similar to what has been observed in related nanosheet systems.^{46–51} By solving the Bragg equation for the indexed peaks, one calculates a repeat distance of 1.72 ± 0.12 nm of the sheets. This value is consistent with the diameter of the TBA cation (~ 1.0 nm) in the interlayer spaces and the crystallographic nanosheet thickness (0.5 nm).⁴⁶ Overall, the data in Figure 2C demonstrates that $\text{TBA}_2\text{Ti}_4\text{O}_9$ forms nanosheet stacks upon drying, with no registry among sheets in the different layers.

Based on electron microscopy data, both $\text{K}_2\text{Ti}_4\text{O}_9$ and $\text{H}_2\text{Ti}_4\text{O}_9$ form needles approximately 500 nm thick

- (44) Suzuki, S.; Miyayama, M. *J. Phys. Chem. B* **2006**, *110*(10), 4731–4734.
- (45) He, M.; Feng, X.; Lu, X. H.; Ji, X. Y.; Liu, C.; Bao, N. Z.; Xie, J. W. *J. Mater. Sci.* **2004**, *39*(11), 3745–3750.
- (46) Sasaki, T.; Watanabe, M.; Hashizume, H.; Yamada, H.; Nakazawa, H. *J. Am. Chem. Soc.* **1996**, *118*(35), 8329–8335.
- (47) Nakato, T.; Miyamoto, N.; Harada, A.; Ushiki, H. *Langmuir* **2003**, *19*(8), 3157–3163.
- (48) Akatsuka, K.; Takanashi, G.; Ebina, Y.; Sakai, N.; Haga, M.; Sasaki, T. *J. Phys. Chem. Solids* **2008**, *69*(5–6), 1288–1291.
- (49) Sakai, N.; Fukuda, K.; Omoto, Y.; Ebina, Y.; Takada, K.; Sasaki, T. *J. Phys. Chem. C* **2008**, *112*(13), 5197–5202.
- (50) Li, L.; Ma, R. Z.; Ebina, Y.; Fukuda, K.; Takada, K.; Sasaki, T. *J. Am. Chem. Soc.* **2007**, *129*(25), 8000–8007.
- (51) Ebina, Y.; Sasaki, T.; Harada, M.; Watanabe, M. *Chem. Mater.* **2002**, *14*(10), 4390–4395.

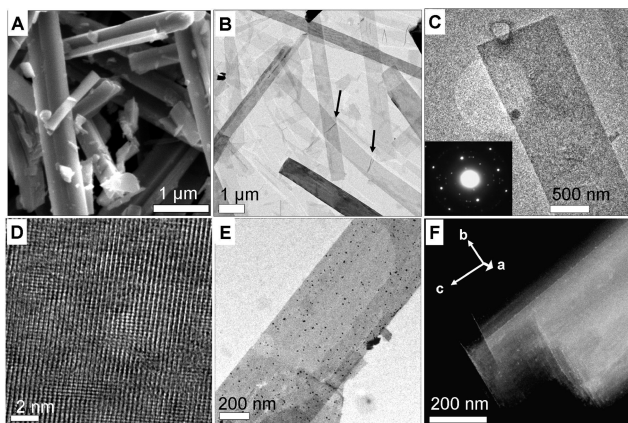


Figure 3. (A) SEM of $\text{H}_2\text{Ti}_4\text{O}_9$. (B–D) TEMs of $\text{TBA}_2\text{Ti}_4\text{O}_9$ nanosheets. Arrows in B indicate folds. (C) A single ribbon with SAED pattern (inset). (D) HR-TEM of a single $\text{TBA}_2\text{Ti}_4\text{O}_9$ nanosheet viewed from [100] direction. (E) Pt-modified $\text{TBA}_2\text{Ti}_4\text{O}_9$ nanosheets. (F) STEM of $\text{Pt}@\text{K}_2\text{Ti}_4\text{O}_9$. Pt nanoparticles are visible as white dots.

and up to several micrometers long, whose principle growth direction coincides with c axis of the crystal (Figure S1 in the Supporting Information and Figure 3A). Upon exfoliation, these needles cleave into ribbons (Figure 3B). On the basis of the contrast in the bright-field TEM, the great majority of these ribbons are single nanosheets. A few multisheet ribbons appear darker in the TEM, and some ribbons become folded, as they deposit onto the TEM grid. Selected area electron diffraction (inset in Figure 3C) confirms that the ribbons are terminated by (100) planes on the top and bottom. This is consistent with the cleavage of the needles during exfoliation along the K^+ interlayer, which coincides with (100) planes. A high-resolution electron micrograph of the ribbons (Figure 3D) reveals two sets of lattice fringes: a set of major ones perpendicular to the length of the ribbons and another set of minor fringes parallel to it. The major fringes with 3.5 \AA spacing arise from the apparent Ti–Ti separation in the c direction. This is not the actual Ti–Ti vector connecting edge-shared TiO_6 octahedra but the projection of it in the [100] direction. The minor fringes ($\sim 2.6 \text{ \AA}$ apart), on the other hand, originate from Ti–Ti separations between edge-shared octahedra in the b direction.

In accordance with observations for rutile and anatase,⁵² infrared spectra of $\text{K}_2\text{Ti}_4\text{O}_9$ (Figure 4A) contain bands in the 800 – 400 cm^{-1} region that can be assigned to Ti–O vibrations. Overall, nine distinct bands can be distinguished in the data for $\text{K}_2\text{Ti}_4\text{O}_9$. This agrees with the number of different chemical environments of Ti–O sites in the compound. $\text{K}_2\text{Ti}_4\text{O}_9$ contains four different Ti sites and nine different O sites in either terminal or bridging (μ_2 , μ_3 , μ_4) configurations. Because a detailed analysis of the vibrational modes of the compound is beyond the scope of this paper, we tentatively assign the highest energy vibration (939 cm^{-1}) to terminal O–Ti bonds, those with intermediate energies (854 – 557 cm^{-1}) to μ_2 -O–Ti bonds, and those of lowest energy (486 – 440 cm^{-1}) to μ_3 -O–Ti and μ_4 -O–Ti bonds. This assignment is

- (52) Ocana, M.; Garciamos, J. V.; Serna, C. J. *J. Am. Ceram. Soc.* **1992**, *75*(7), 2010–2012.

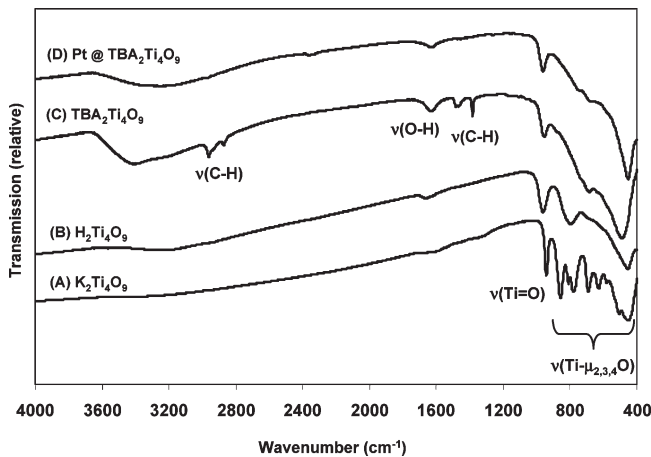


Figure 4. IR spectra of (A) K₂Ti₄O₉, (B) H₂Ti₄O₉, (C) TBA₂Ti₄O₉, and (D) Pt@TBA₂Ti₄O₉.

consistent with trends observed for terminal and bridging oxygen in metal oxo complexes.⁵³

Upon cation exchange and exfoliation, these bands become broader and coalesce into three (H₂Ti₄O₉) to four (TBA₂Ti₄O₉) bands that partially overlap (Figure 4B/C). The terminal O–Ti bands move to slightly higher energy (955 cm⁻¹ in H₂Ti₄O₉), whereas the μ_4 -O–Ti bands are nearly unchanged. The latter makes sense if one considers that the μ_4 -O sites are buried in the structure and are less accessible to protons and water molecules. Intuitively, one would expect the terminal O–Ti vibration to shift to higher energy upon protonation. However, for polyoxovanadates⁵⁴ and polyoxoniobates⁵⁵ it is known that terminal oxide ions are harder to protonate than μ_2 -O and μ_3 -O ions. For Ti₄O₉²⁻, this means that the terminal oxide likely remains nonprotonated. The shift of the corresponding vibration to higher energy is then the result of increasing Ti=O double-bond character because of the reduction of electron donor strength of the protonated μ_2 -O and μ_3 -O sites. Such proton-induced withdrawal of electron density at distant O sites is supported by NMR studies with polyoxovanadates.⁵⁴ In TBA₂Ti₄O₉ (943 cm⁻¹), the blue shift of the terminal O–Ti band is diminished and the band is weaker. This could be due to either interactions with the water or partial loss of terminal oxo-groups, as observed for the related (110) rutile–TiO₂ surface.⁵⁶

Figure 4D also shows the IR spectrum of nanosheets after photochemical deposition of Pt in aqueous methanol solution. As most notable change, the C–H bands in this material have disappeared, indicating that the TBA counterion has been displaced by other ions (H⁺, Pt²⁺).

Diffuse reflectance spectra for K₂Ti₄O₉ and derivatives are shown in Figure 5. K₂Ti₄O₉ itself has an absorption

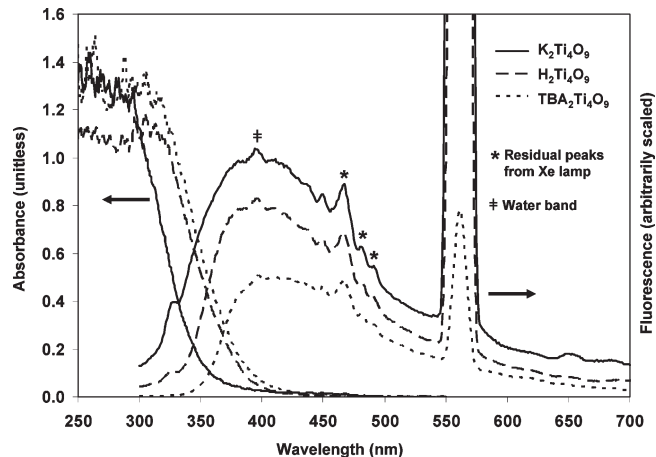


Figure 5. Diffuse reflectance UV–vis and fluorescence spectra ($\lambda_{\text{ex}} = 280 \text{ nm}$) for K₂Ti₄O₉, H₂Ti₄O₉, and TBA₂Ti₄O₉. Arrows indicate respective Y-axes.

edge at $\sim 350 \text{ nm}$, in accordance with a 3.54 eV bandgap. Upon proton incorporation, the edge moves to 375 nm (3.31 eV) and a further red shift to 382 nm (3.25 eV) occurs upon exfoliation into TBA₂Ti₄O₉.

Fluorescence spectra (Figure 5) show a similar trend. For K₂Ti₄O₉, a broad emission is observed at 400 nm, whereas for H₂Ti₄O₉ and TBA₂Ti₄O₉, the emission maxima occur at 400 and 413 nm. In addition, the width of the emission bands becomes smaller for K₂Ti₄O₉ (155 nm), H₂Ti₄O₉ (133 nm), and (TBA)₂Ti₄O₉ (130 nm), judged from the full width at half-maximum (fwhm, values in brackets). Together with the absorption data, this confirms a reduction of the bandgap of the semiconductors in the order K₂Ti₄O₉ (3.54 eV) > H₂Ti₄O₉ (3.25 eV) > TBA₂Ti₄O₉ (3.00 eV). This trend is very similar to what we recently observed in the series K₄Nb₆O₁₇ > H₂K₂Nb₆O₁₇ > nano-TBA₄Nb₆O₁₇.³

We attribute this band gap reduction to two main factors: The change in chemical composition of the phases and second, the introduction of defects upon exfoliation. The most significant lowering of ΔE occurs in going from K₂Ti₄O₉ to H₂Ti₄O₉. This is in line with predictions by DiQuarto et al. who show that the bandgap of metal oxides increases with the square of the difference of Pauling electronegativities (EN) of the metal and oxygen components.⁵⁷ Applied to the titanate system studied here, this means that replacement of potassium (EN = 0.8) with hydrogen (EN = 2.2) whose EN is more comparable to oxygen (EN = 3.5) leads to a reduction of the bandgap. A similar argument can be made for the couple K₄Nb₆O₁₇/H₂K₂Nb₆O₁₇, mentioned above. An additional bandgap reduction occurs upon exfoliation of the metal oxides into nanosheets. This reduction may be attributed to the formation of structural defects along the nanosheet edges and also on the nanosheet surface.

To determine the photocatalytic properties of the titanates, we irradiated dispersions of 100 mg of each material in pure water with light from two to four 175 W

- (53) Nakamoto, K. *Infrared and Raman Spectra of Inorganic and Coordination Compounds*, 5th ed.; Wiley: New York, 1997.
- (54) Day, V. W.; Klempner, W. G.; Maltbie, D. J. *J. Am. Chem. Soc.* **1987**, *109*(10), 2991–3002.
- (55) Black, J. R.; Nyman, M.; Casey, W. H. *J. Am. Chem. Soc.* **2006**, *128*(45), 14712–14720.
- (56) Wendt, S.; Sprunger, P. T.; Lira, E.; Madsen, G. K. H.; Li, Z. S.; Hansen, J. O.; Matthiesen, J.; Blekinge-Rasmussen, A.; Laegsgaard, E.; Hammer, B.; Besenbacher, F. *Science* **2008**, *320*(5884), 1755–1759.

- (57) DiQuarto, F.; Sunseri, C.; Piazza, S.; Romano, M. C. *J. Phys. Chem. B* **1997**, *101*(14), 2519–2525.

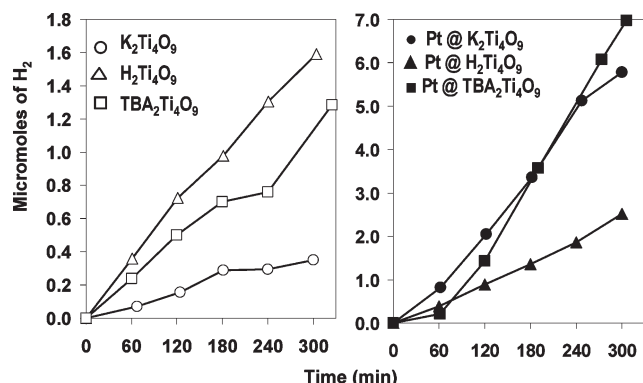


Figure 6. Measured photochemical hydrogen production from water. Conditions: 100 mg of each material in 50 mL degassed water, four 175 W Hg arc lamps (two 175 W lamps for platinated materials).

low-pressure mercury arc lamps. The gas space above was sampled periodically. For $\text{K}_2\text{Ti}_4\text{O}_9$, $\text{H}_2\text{Ti}_4\text{O}_9$, and $\text{TBA}_2\text{Ti}_4\text{O}_9$, only very small amounts of H_2 were detected after 5 h of irradiation ($< 0.5 \mu\text{mol}/\text{h}$), and during some runs no H_2 was measured at all (Figure 6). This establishes these metal oxides as not active for photocatalytic water splitting.

As photoelectrochemical Pt deposition is known to enhance the photocatalytic properties of metal oxides,¹ 2% (mass) platinum was deposited onto the titanates by photolysis of solution of the respective metal oxide in 20% (v/v) $\text{CH}_3\text{OH}/\text{H}_2\text{O}$. In the case of $\text{K}_2\text{Ti}_4\text{O}_9$ (Figure 3F), small ($< 10 \text{ nm}$) Pt particles form preferentially on the (001) and (010) facets of the crystals. Relatively few particles are found on the (100) facets, which coincide with the titanate layer plane. Apparently, the rougher edges of layers provide better growth sites for the Pt nanoparticles. Under similar deposition conditions, $\text{TBA}_2\text{Ti}_4\text{O}_9$ nanosheets deposit small ($5.77 \pm 1.73 \text{ nm}$) Pt clusters evenly on the (100) surface (Figure 3E), with no evidence for preferential deposition at the nanosheet periphery as previously observed in the related $(\text{TBA})\text{Ca}_2\text{Nb}_3\text{O}_{10}$ nanosheets.⁷ The puckered surface of the titanate nanosheets seems to provide good metal adhesion sites.

After Pt modification, the H_2 evolution rate from water increases slightly but remains below $1.5 \mu\text{mol}/\text{h}$, even for the most active material. This and the lack of detectable O_2 show that platination does not activate the titanates toward water splitting.

To gain further insight into the photochemical properties of the titanates, we carried out additional irradiation studies in the presence of sacrificial electron donors (methanol)⁵⁸ and acceptors (AgNO_3).⁵⁹ The results are shown in Figure 7 and in Table 1. As can be seen from Figure 7, all titanates evolve H_2 steadily from aqueous methanol solutions.

On the basis of equal mass (100 mg), the catalytic activity of the nonplatinated materials decreases in the

order $\text{H}_2\text{Ti}_4\text{O}_9$ ($29 \mu\text{mol}/\text{h}$), $\text{TBA}_2\text{Ti}_4\text{O}_9$ ($14 \mu\text{mol}/\text{h}$), and $\text{K}_2\text{Ti}_4\text{O}_9$ ($4 \mu\text{mol}/\text{h}$). However, on the basis of equal molar amounts (1 mmol) of catalysts (see caption for Table 1), one obtains the following order: $\text{TBA}_2\text{Ti}_4\text{O}_9$ ($115 \mu\text{mol}/\text{h}$), $\text{H}_2\text{Ti}_4\text{O}_9$ ($98 \mu\text{mol}/\text{h}$), and $\text{K}_2\text{Ti}_4\text{O}_9$ ($17 \mu\text{mol}/\text{h}$), i.e., $\text{TBA}_2\text{Ti}_4\text{O}_9$ is the most active catalyst.

After platination, the activity increases by up to 55 times, with $\text{Pt}@\text{TBA}_2\text{Ti}_4\text{O}_9$ being the most active ($405 \mu\text{mol}/\text{h}$), followed by $\text{Pt}@\text{H}_2\text{Ti}_4\text{O}_9$ ($252 \mu\text{mol}/\text{h}$), and $\text{Pt}@\text{K}_2\text{Ti}_4\text{O}_9$ ($221 \mu\text{mol}/\text{h}$). The observed activity trend agrees well with the relative positions of the conduction band edges of the platinated catalysts, as will be detailed below.

When the platinated catalysts were irradiated in 0.01 M AgNO_3 solution, only small quantities of O_2 were evolved. Essentially the order of activities was reversed from the H_2 evolution, with $\text{Pt}@\text{TBA}_2\text{Ti}_4\text{O}_9$ now being the least active ($1.8 \mu\text{mol}/\text{h}$), followed by $\text{Pt}@\text{H}_2\text{Ti}_4\text{O}_9$ ($2.1 \mu\text{mol}/\text{h}$) and with $\text{Pt}@\text{K}_2\text{Ti}_4\text{O}_9$ ($3.5 \mu\text{mol}/\text{h}$) as the most active material.

An understanding of the photocatalytic properties of the titanates cannot be achieved without knowledge of their band edge energies, which determine the electrochemical potentials of photogenerated electrons and holes. For nanomaterials, these data are difficult to gather from electrochemical impedance spectroscopy because of the complexity of the charge transfer characteristics of nanostructured electrodes.⁶⁰ However, the conduction band edge of semiconductor electrode can be approximated by measuring the onset potential for the anodic photocurrent.^{48,61,62} Consequently, photoelectrochemical measurements were conducted with the titanates in the presence of methanol as a sacrificial electron donor, and 0.25 M sodium dihydrogen phosphate as pH buffer. Representative potential current curves recorded under chopped illumination are shown for $\text{TBA}_2\text{Ti}_4\text{O}_9$ and $\text{Pt}@\text{TBA}_2\text{Ti}_4\text{O}_9$ films in Figure 8.

It can be seen that the anodic photocurrents due to the oxidation of methanol are very small ($< 1.0 \mu\text{A}/\text{cm}^2$) and diminish in magnitude as the potential is scanned in cathodic direction. For $\text{TBA}_2\text{Ti}_4\text{O}_9$ and $\text{Pt}@\text{TBA}_2\text{Ti}_4\text{O}_9$, respectively, the onset potentials (vertical arrows in Figure 8) occur at approximately -0.525 V and -0.30 V (NHE).

Data for the remaining compounds (see Figures S2–S4 in the Supporting Information) in connection with the optical band gaps from Figure 5 were taken to obtain the edge potentials shown in Figure 9.

Interestingly, the measured conduction band edges for most titanates are quite low and barely reach the thermodynamic proton reduction potential at neutral pH

(58) Domen, K.; Kudo, A.; Shibata, M.; Tanaka, A.; Maruya, K.; Onishi, T. *J. Chem. Soc., Chem. Commun.* **1986**, 23, 1706–1707.
 (59) Domen, K.; Yoshimura, J.; Sekine, T.; Tanaka, A.; Onishi, T. *Catal. Lett.* **1990**, 4(4–6), 339–343.

(60) Morrison, S. R., *Electrochemistry at Semiconductor and Oxidized Metal Electrodes*; Plenum Press: New York, 1980; p xiv, 401.
 (61) Bard, A. J.; Faulkner, L. R., *Electrochemical Methods: Fundamentals and Applications*, 2nd ed.; John Wiley: New York, 2001; p 754.
 (62) Ishikawa, A.; Takata, T.; Kondo, J. N.; Hara, M.; Kobayashi, H.; Domen, K. *J. Am. Chem. Soc.* **2002**, 124(45), 13547–13553.

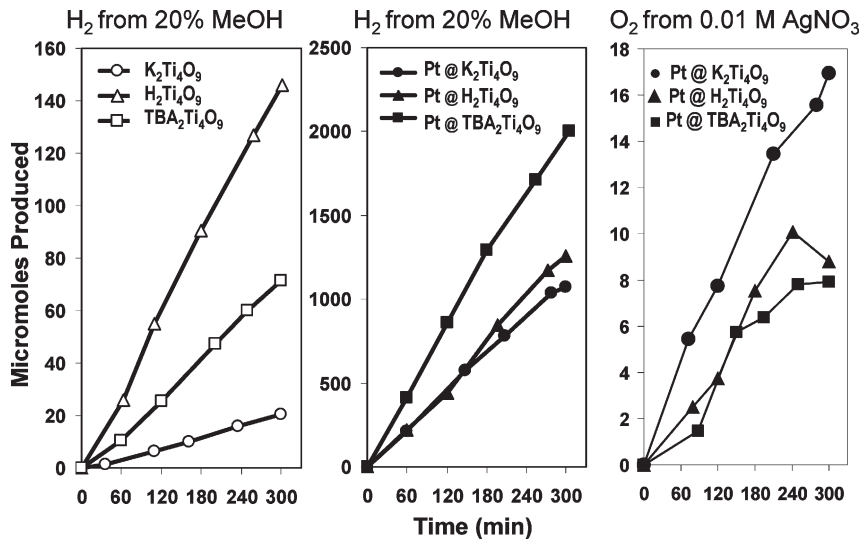


Figure 7. H_2 and O_2 evolution from aqueous solutions of sacrificial electron donors and acceptors. Conditions: 100 mg of catalyst, 300 W Xe-arc lamp, 50 mL of degassed aqueous methanol (20% vol) or 0.01 M AgNO_3 solution.

Table 1. H_2 and O_2 Evolution Results^a

catalyst	amount (mg)	20% (v/v) methanol/water			0.01 M aq AgNO_3		
		solution pH	H_2 ($\mu\text{mol}/\text{h}$)	H_2 after 5 h (micromol)	solution pH	O_2 ($\mu\text{mol}/\text{h}$)	O_2 after 5 h (micromol)
$\text{K}_2\text{Ti}_4\text{O}_9$	100	10.7–11.0	4 (17) ^b	10			
$\text{H}_2\text{Ti}_4\text{O}_9$	100	4.0–4.8	29 (98) ^b	147			
$\text{TBA}_2\text{Ti}_4\text{O}_9$	100	9.0–9.9	14 (115) ^b	71			
Pt@ $\text{K}_2\text{Ti}_4\text{O}_9$	100	3.4–4.0	221	1106	2.4	3.5	17.6
Pt@ $\text{H}_2\text{Ti}_4\text{O}_9$	100	3.5–4.3	252	1262	2.4–2.5	2.1	10.5
Pt@ $\text{TBA}_2\text{Ti}_4\text{O}_9$	100	3.6–4.5	405	2027	2.6–2.8	1.8	8.9

^a Conditions: 100 mg of catalyst, 300 W Xe-arc lamp, 50 mL of degassed aqueous methanol (20% vol) or 0.01 M AgNO_3 solution. ^b H_2 rates in brackets are per millimole of catalyst, $\text{H}_2\text{Ti}_4\text{O}_9$ ($M = 337.6 \text{ g/mol}$), $\text{K}_2\text{Ti}_4\text{O}_9$ ($M = 413.8 \text{ g/mol}$), $\text{TBA}_2\text{Ti}_4\text{O}_9$ ($M = 820.4 \text{ g/mol}$).

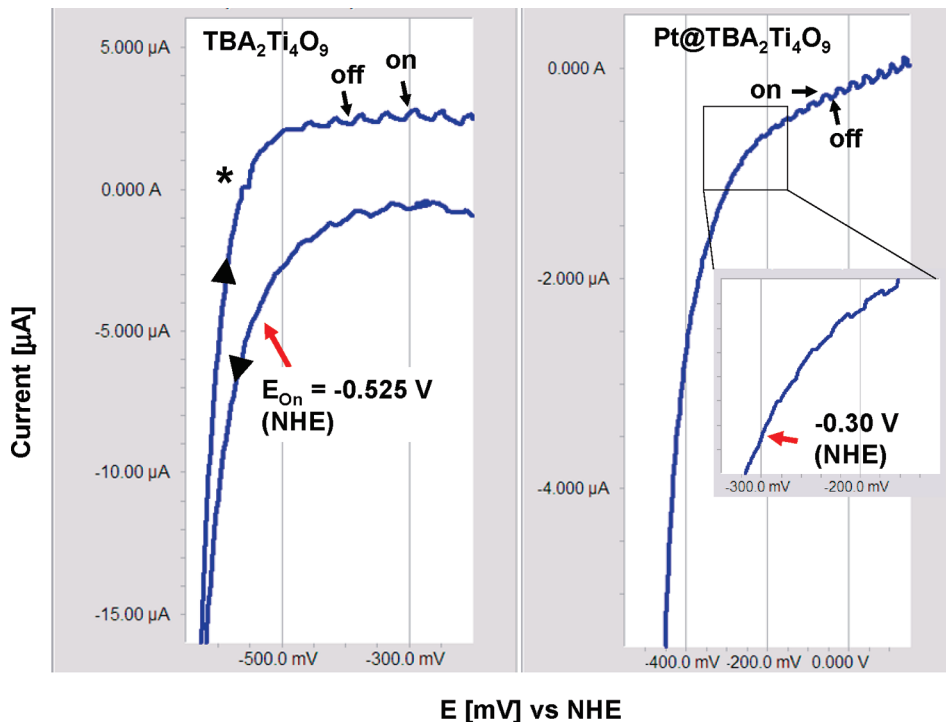


Figure 8. Cyclic voltammograms for $\text{TBA}_2\text{Ti}_4\text{O}_9$ and $\text{Pt}@\text{TBA}_2\text{Ti}_4\text{O}_9$ films on gold electrode under chopped UV light (200–380 nm, 15 mW/cm²) in 0.25 M phosphate buffer at pH 7 with 10% methanol as sacrificial electron donor. Arrows on $\text{TBA}_2\text{Ti}_4\text{O}_9$ data indicate scan direction (10 mV/s).

(−0.41 V). We believe that this band edge depression is partially caused by adsorption of sodium ions (from

the 0.25 M $\text{Na}_2\text{HPO}_4/\text{NaH}_2\text{PO}_4$ buffer) to the titanates. The effect of potential-determining ions on the flatband

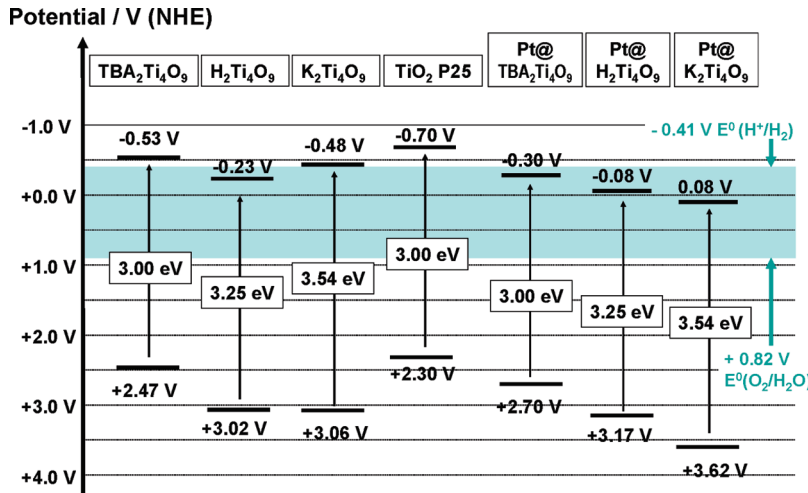


Figure 9. Band edge potentials from optical and photoelectrochemical measurements. All values given versus NHE at pH 7. Experimental data for TiO_2 nanoparticles (Degussa P25) are included for comparison. The gray band indicates theoretical water oxidation and reduction potentials at pH 7.

potential of semiconductors is well-documented.^{63–66} In the following discussion, we assume that the effect of K^+ is approximately constant across the series, and that the observed differences in the conduction band edges for the different materials are significant.

Among nonplatinated materials, $\text{TBA}_2\text{Ti}_4\text{O}_9$ has the most reducing edge, followed by $\text{K}_2\text{Ti}_4\text{O}_9$ and $\text{H}_2\text{Ti}_4\text{O}_9$. Thus, one expects $\text{TBA}_2\text{Ti}_4\text{O}_9$ to be the most active catalyst for the Hydrogen Evolution Reaction (HER) from aqueous methanol, followed by $\text{K}_2\text{Ti}_4\text{O}_9$ and then $\text{H}_2\text{Ti}_4\text{O}_9$. Experimentally, we do indeed find $\text{TBA}_2\text{Ti}_4\text{O}_9$ to be most active catalyst (based on equal molar amounts of catalysts, Table 1), but $\text{H}_2\text{Ti}_4\text{O}_9$ is six times more active than $\text{K}_2\text{Ti}_4\text{O}_9$. We attribute this deviation to the greater acidity of the $\text{H}_2\text{Ti}_4\text{O}_9$ phase, which lowers the pH value of the reaction mixture during the catalytic test (Table 1). We had previously observed that the H_2 evolution activity of niobates increases with lower solution pH.⁷ The same seems to be the case with the titanates.

Among the platinated materials, the conduction and valence band edges are correlated directly with the observed H_2 and O_2 evolution rates in the presence of sacrificial agents. Here we find that the more reducing the conduction band edge, the more H_2 is evolved from aqueous methanol, and the more oxidizing the valence band edge, the more O_2 is evolved. The band edge energies in Figure 9 also explain why the most active H_2 producers are the least active O_2 producers and vice versa.

Interestingly, the measured conduction band edges of the platinated materials are all significantly decreased from the values for the unmodified titanates. The band shift varies from +150 mV for $\text{H}_2\text{Ti}_4\text{O}_9$ to up to +660 mV for $\text{K}_2\text{Ti}_4\text{O}_9$. This suggests that the Pt particles are

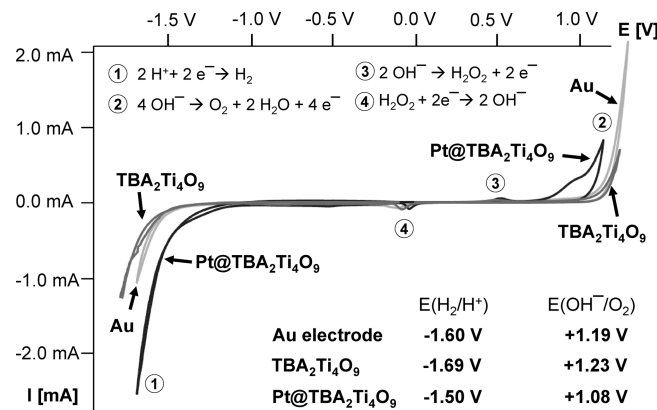


Figure 10. (A) Cyclic voltammograms (100 mV/s) of $\text{TBA}_2\text{Ti}_4\text{O}_9$ and $\text{Pt}@\text{TBA}_2\text{Ti}_4\text{O}_9$ films on Au disk electrode in aqueous 1.0 M $\text{TBA}(\text{OH})$ solution at pH 14. All potentials are reported versus NHE. The current–potential curve for a clean Au electrode is also shown. Onset potentials are determined at ± 0.5 mA respectively.

polarizing the titanates positively. This polarization could occur as a result of Fermi level equilibration between Pt and nanosheet, as observed in Schottky-type contacts. Because the Pt Fermi energy (+1.2 V NHE) is below the conduction band edges of the titanates, electrons flow from the titanate to the Pt particles. In theory, this junction aids the flow of electrons toward the titanate–platinum interface, whereas holes are repelled from it and move in the opposite direction. The polarization may also be due the absorption of nonreduced Pt^{2+} ions during the photochemical platination procedure. Based on the IR spectrum (Figure 4D), TBA is no longer present in platinated $\text{TBA}_2\text{Ti}_4\text{O}_9$. This indicates that TBA cation has been replaced either by Pt^{2+} ions or by protons. We are presently unable to distinguish between these possibilities.

To determine the effect of platination on the redox properties of the titanate nanosheets, cyclic voltammograms were recorded for films of platinated and nonplatinated $\text{TBA}_2\text{Ti}_4\text{O}_9$ in aqueous $\text{TBA}(\text{OH})$ solution at pH 14. From Figure 10, it can be seen that for $\text{TBA}_2\text{Ti}_4\text{O}_9$, the onset for water oxidation occurs at $E = +1.23$ V and

- (63) Frese, K. W. *J. Appl. Phys.* **1982**, *53*(3), 1571–1576.
- (64) Frese, K. W.; Canfield, D. G. *J. Electrochem. Soc.* **1984**, *131*(11), 2614–2618.
- (65) Kocha, S. S.; Turner, J. A. *J. Electrochem. Soc.* **1995**, *142*(8), 2625–2630.
- (66) Hilal, H. S.; Turner, J. A. *Electrochim. Acta* **2006**, *51*(28), 6487–6497.

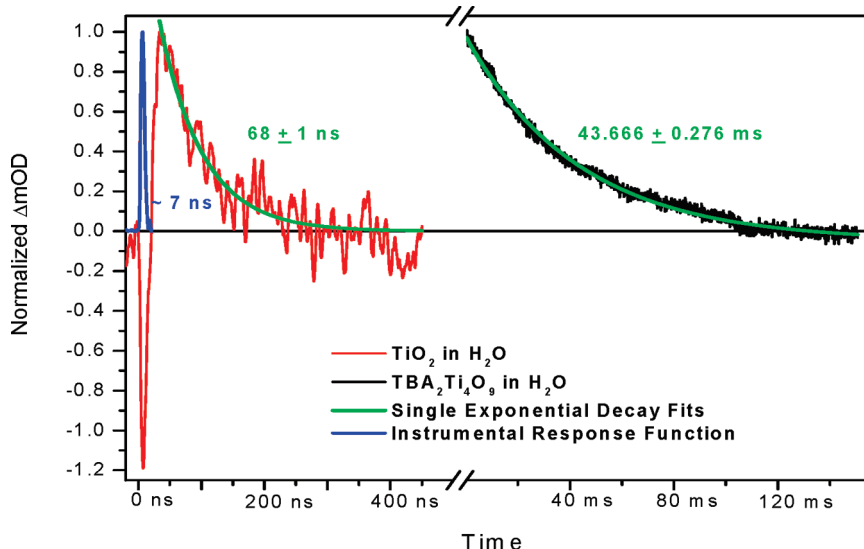


Figure 11. Transient absorption for TBA₂Ti₄O₉ and TiO₂ in H₂O (pumped at 266 nm and probed at 658 nm). TiO₂ and TBA₂Ti₄O₉ exhibit exponential decays of 68 ± 1 ns and 43.666 ± 0.276 ms with R^2 values of 0.86 and 0.99, respectively. The signal magnitudes were 28 and 61 mOD. The instrument response function associated with the system is estimated at 7 ns (full width at half-maximum) as obtained via scattering of the 266 nm pump light into the detector. The negative signal at early times of the TiO₂ curve is a result of residual pump scatter.

for water reduction at $E = -1.69$ V. These values are +0.83 V above and −0.86 V below the thermodynamic potentials at this pH ($E_{\text{ox}} = +0.40$ V, $E_{\text{red}} = -0.83$ V), which demonstrates that TBA₂Ti₄O₉ nanosheets are a poor catalyst for water electrolysis. After platination, however, these overpotentials are reduced somewhat and hydrogen evolution now takes place at $E_{\text{red}} = -1.50$ V. This shows that water reduction now at least partially occurs on the Pt surface, which is among the most active catalysts for the hydrogen evolution reaction (HER).⁶⁷ This effect on the proton reduction potential is also observed in platinumated TBACa₂Nb₃O₁₀ nanosheets.⁵ In addition, platination also seems to reduce the TBA₂Ti₄O₉ overpotential for O₂ evolution, which can be observed by the shift of the anodic current onset from +1.23 V to +1.08 V. This greater ease for O₂ evolution agrees well with the Pt-induced lowering of the valence band edge (Figure 9) as deduced from the photoelectrochemical measurements. As Pt reduces the negative charge on the nanosheets, the oxidation of water is favored both thermodynamically and kinetically, as the penetration of hydroxide into the nanosheet film becomes easier.

The electron–hole recombination kinetics of TBA₂Ti₄O₉ nanosheets were resolved with transient absorption (pump–probe) spectroscopic measurements on suspensions in water. It is well-known that for metal oxides, electrons trapped in mid gap states give rise to a broad absorption with a maximum around 600 nm and extending to the 658 nm wavelength of the applied probe light.⁶ Following direct excitation at 266 nm, well into the band gap of the studied systems, the resulting decay of the absorption of the electron population for TBA₂Ti₄O₉ nanosheets is shown in Figure 11. A single exponential fit to this data yields a time-constant of $43.666 \pm$

0.276 ms. Under near identical conditions, the kinetics observed in suspended TiO₂ nanocrystals (Degussa P25) exhibit a 68 ± 1 ns time constant decay that is approximately 6 orders of magnitude faster. While this is the first report of long time dynamics associated with TBA₂Ti₄O₉ nanosheets, the nanosecond TiO₂ recombination kinetics observed here are similar to previous studies.^{68,69} Recently, Klug⁷⁰ and co-workers reported that low excitation density, $0.6 \mu\text{J}/\text{mm}^2$, retards electron–hole recombination even on the microsecond time scale in TiO₂ compared with studies conducted at higher fluxes. The excitation densities used in this study are 3 orders of magnitude higher, yet the electron decay rate associated with the nanosheets is considerably longer compared with TiO₂. The slower kinetics observed for the TBA₂Ti₄O₉ nanosheets originate either from the presence of deeper trap sites on the sheets vs the nanoparticles or from more effective electron–hole separation because of the micrometer dimensions of the 2D lattice.

Conclusion

In summary, we have systematically studied the evolution of the optical, vibrational, electronic, and photocatalytic properties of several layered titanates A₂Ti₄O₉ (A = K, H, TBA) and the nanoribbons derived from these. All compounds are catalysts for photochemical H₂ and O₂ evolution from solutions of sacrificial electron donors, but not from water. The activities vary only slightly in going from the condensed phases to the nanoribbons, which indicates that excitation, charge separation, and water activation are localized processes that do not involve charge transfer between titanate layers. Cation exchange and

(68) Serpone, N.; Lawless, D.; Khairutdinov, R.; Pelizzetti, E. *J. Phys. Chem.* **1995**, 99(45), 16655–16661.

(69) Leytner, S.; Hupp, J. T. *Chem. Phys. Lett.* **2000**, 330(3–4), 231–236.

(70) Tang, J. W.; Durrant, J. R.; Klug, D. R. *J. Am. Chem. Soc.* **2008**, 130(42), 13885–13891.

exfoliation perturb the electronic structure of the titanate nanosheets to some extent and reduce the optical bandgap at each reaction step. This is the result of both the changing chemical composition of the materials and the formation of defects along the nanosheet edges. These defects may also be responsible for the trapping of photogenerated electrons, which decay on the millisecond time scale, compared to nanoseconds for TiO_2 nanocrystals. On the basis of photoelectrochemical measurements, the catalytic activity of all titanates in the series is limited by the potential of the conduction band edge, which is too low for efficient proton reduction in neutral solution. Photochemical platination shifts the band edge of all titanates to more oxidizing potentials, which we attribute to Fermi level equilibration across the titanate–platinum interface.

Experimental Section

Reagents were used as received without further purification (TiO_2 anatase, 99.8% purity, Aldrich; K_2CO_3 , >99% purity, Acros; tetrabutyl ammonium hydroxide, 40% in water, Acros; and $\text{H}_2\text{PtCl}_6 \cdot 6\text{H}_2\text{O}$, 99.9% purity, Acros). Water was purified to >18 $\text{M}\Omega \text{ cm}$ using a Nanopure system. Unless otherwise specified, annealings and reactions were performed under ambient conditions. Powder X-ray diffraction data were obtained using a Scintag XDS-2000 X-ray powder diffractometer using $\text{Cu K}\alpha$ radiation. TEM micrographs were obtained using a Philips CM 120 microscope and SEM micrographs were obtained using a FEI XL30-SFEG microscope. HR-TEM and STEM micrographs were obtained using a JEOL 2500SE 200 kV microscope. For platinum photodeposition, a 300 W Xe-arc lamp (Cermax PE300 BUV) was used. Gas analysis was performed with a Varian 3800 gas chromatograph employing a TCD detector.

Synthesis of $\text{K}_2\text{Ti}_4\text{O}_9$ and $\text{H}_2\text{Ti}_4\text{O}_9$. $\text{K}_2\text{Ti}_4\text{O}_9$ and $\text{H}_2\text{Ti}_4\text{O}_9$ were synthesized according to the literature.⁴⁵ Briefly, K_2CO_3 and TiO_2 were ground together in a 1:3 molar ratio, pressed into pellets, and annealed at 960 °C for 10 h. The identity of $\text{K}_2\text{Ti}_4\text{O}_9$ was confirmed with XRD. For the synthesis of $\text{H}_2\text{Ti}_4\text{O}_9$, 3.0 g of the white powder was stirred in 250 mL of 1.0 M HCl (10-fold molar excess) for 24 h at room temperature. The titanate was then centrifuged out of solution, added to a fresh HCl solution of equal concentration, and stirred for an additional 24 h, after which it was washed multiple times with water and dried in vacuo (82% yield).

Exfoliation of $\text{H}_2\text{Ti}_4\text{O}_9$ into Colloidal Sheets. $\text{H}_2\text{Ti}_4\text{O}_9$ (1.5 g) was dissolved in 175 g of an aqueous solution of 13.3% (w) TBA(OH) and gently heated to ~70 °C under nitrogen while stirring for 7.5 days. The resulting colloidal sheets were centrifuged out of solution, washed twice with water to remove excess TBA(OH), and then redispersed in water, maintaining a pH > 8 to ensure exfoliation.

2% Pt Loading. All platinum deposition reactions were performed by dissolving 100 mg of catalyst in 75 mL of 20% (v/v) methanol/water solution containing 5.3 mg $\text{H}_2\text{PtCl}_6 \cdot 6\text{H}_2\text{O}$ (2 mg Pt). The solution was purged with argon, then irradiated with a 300 W Xe arc lamp for 1 h while stirring. The resultant brown-white precipitate was centrifuged out of solution, washed four times with water, and resuspended into water to ensure that methanol was fully removed.

Irradiation Experiments. All samples for photolytic experiments were prepared by dissolving 100 mg of the respective materials in 50 mL of purified water. The solution was transferred into a 100 mL round-bottom quartz flask, attached to airtight gas line system, and purged of atmospheric gases by sequentially evacuating the flask and refilling with argon (5 min, 760 Torr). After five such cycles, the solution was allowed to stir for 30 min at 760 Torr. An aliquot of gas above the solution was then directly injected into a gas chromatograph (Varian 3800) via the gas line to verify the absence of H_2 , O_2 , and N_2 . The homogeneous catalyst solutions were then stirred and irradiated with 175 W Hg arc lamps for water photolysis experiments (see caption of Figure 6), and with one 300 W Xe arc lamp for experiments with sacrificial reagents. Gas aliquots were taken hourly above the solution and quantitatively analyzed for their H_2 , O_2 , and N_2 content with the GC.

Electrochemical measurements were conducted in 0.25 M $\text{Na}_2\text{HPO}_4/\text{NaH}_2\text{PO}_4$ buffer solution at pH 7. Titanates were deposited onto gold electrodes (1 cm^2) as aqueous dispersions and left to dry in a nitrogen stream. The electrochemical cells consisted of a Pt counter electrode and a calomel reference electrode that was connected to the cell via a KCl saltbridge. The cell was calibrated using the redox potential of $\text{K}_4[\text{Fe}(\text{CN})_6]$ at +0.358 V (NHE). Photoelectrochemical measurements were performed similarly, using irradiation from a 300 W Xe arc lamp, equipped with a water IR filter, and a fiber optics cable that delivered an irradiance of 15 mW/cm^2 at 200–380 nm to the working electrode.

For transient absorption measurements, samples of $\text{TBA}_2\text{Ti}_4\text{O}_9$ and TiO_2 nanocrystals (Degussa P25) were prepared at concentrations of 0.890 mg/g and 0.301 mg/g in water correspondingly. Samples were flowed through a commercial 1.0-mm path length quartz cuvette (Starna Inc.). The electronically detected pump–probe setup utilized the fourth harmonic of a Nd:YAG laser (Polaris II New Wave Research) as the pump source, impinging 266 nm light of 112 $\mu\text{J}/\text{pulse}$ at 4 Hz and 153 $\mu\text{J}/\text{pulse}$ at 18 Hz on the $\text{TBA}_2\text{Ti}_4\text{O}_9$ and TiO_2 nanostructure samples respectively. The corresponding pulse fluencies were 143 and 195 $\mu\text{J}/\text{mm}^2$, similar to those used by Hoffmann⁷¹ et al. A temperature and current regulated 658 ± 4 nm continuous wave diode (TCLDM9 Thorlabs) served as the probe, which was isolated from the pump light with long pass ($\lambda > 560$ nm) and band-pass (280 nm < λ < 900 nm) filters. Probe light was detected using a high-speed photodiode (DET10A Thorlabs) that was then amplified 100x times by a DC-coupled wide band preamplifier (BX-31A NF Electronic Instruments) before being digitized via a 1 GHz oscilloscope (TDS 784A Tektronix) and transferred to a computer for further averaging. TiO_2 data were smoothed using ten-point adjacent averaging in Origin. The associated instrument response function is ~7 ns.

Acknowledgment. The authors acknowledge support from the National Science Foundation in the form of an “Energy for Sustainability” grant (CBET 0829142).

Supporting Information Available: SEM data for $\text{K}_2\text{Ti}_4\text{O}_9$ and photoelectrochemical data for $\text{K}_2\text{Ti}_4\text{O}_9$, $\text{Pt}@\text{K}_2\text{Ti}_4\text{O}_9$, $\text{H}_2\text{Ti}_4\text{O}_9$, $\text{Pt}@\text{H}_2\text{Ti}_4\text{O}_9$, TiO_2 (PDF). This material is available free of charge via the Internet at <http://pubs.acs.org>.

(71) Martin, S. T.; Herrmann, H.; Choi, W. Y.; Hoffmann, M. R. *J. Chem. Soc., Faraday Trans.* **1994**, 90(21), 3315–3322.